J. Fluid Mech. (1996), *vol.* 322, *pp.* 51–79

The three-dimensional interaction of a streamwise vortex with a large-chord lifting surface: theory and experiment

By GUSTAVO C. R. BODSTEIN[1], ALBERT R. GEORGE[2] AND C.-Y. HUI[3]

[1] Department of Mechanical Engineering, EE/COPPE/UFRJ, CP 68503, CEP 21945-970, Rio de Janeiro, RJ, Brazil

[2] Mechanical and Aerospace Engineering, Cornell University, Ithaca, NY 14853-7501, USA

[3] Theoretical and Applied Mechanics, Cornell University, Ithaca, NY 14853-7501, USA

(Received 22 March 1994 and in revised form 5 April 1996)

The three-dimensional vortex flow that develops around a close-coupled canard-wing configuration is characterized by a strong interaction between the vortex generated at the canard and the aircraft wing. In this paper, a theoretical potential flow model is devised to uncover the basic structure of the pressure and velocity distributions on the wing surface. The wing is modelled as a semi-infinite lifting-surface set at zero angle of attack. It is assumed that the vortex is a straight vortex filament, with constant strength, and lying in the freestream direction. The vortex filament is considered to be orthogonal to the leading-edge, passing a certain height over the surface. An incompressible and steady potential flow formulation is created based on the three-dimensional Laplace's equation for the velocity potential. The boundary-value problem is solved analytically using Fourier transforms and the Wiener–Hopf technique. A closed-form solution for the velocity potential is determined, from which the velocity and pressure distributions on the surface and a vortex path correction are obtained. The model predicts an anti-symmetric pressure distribution along the span in region near the leading-edge, and a symmetric pressure distribution downstream from it. The theory also predicts no vertical displacement of the vortex, but a significant lateral displacement. A set of experiments is carried out to study the main features of the flow and to test the theoretical model above. The experimental results include helium-soap bubble and oil-surface flow pattern visualization, as well as pressure measurements. The comparison shows good agreement only for a weak interaction case, whereas for the case where the interaction is strong, secondary boundary-layer separation and vortex breakdown are observed to occur, mainly owing to the strong vortex–boundary layer interaction. In such a case the model does not agree well with the experiments.

1. Introduction

Vortex flows occur very often in aerodynamics when vortices are generated and remain in close proximity to the surface of an aircraft configuration. The local surface velocity and pressure distributions and the overall characteristics of the entire configuration are considerably affected by the interaction with these vortices. In general, the vortices produce an extra suction effect on the surface, which increases the lift coefficient up to higher angles of attack than without vortex flow. Typical examples

are the flow around delta wings and the flow around the forebody of a fighter aircraft (Hoeijmakers 1990).

Interaction also occurs when the vortex wake of one component of the aircraft approaches other components, such as the flow around a helicopter blade (blade vortex interaction, BVI), a small aircraft following a large aircraft (wake vortex hazard), and the flow around a close-coupled canard-wing configuration. In the BVI case, vortices are shed continuously from the tips of helicopter blades and are convected downstream past the next approaching blades. Since helicopter blades are very thin and have a large aspect ratio, the pressure changes produced by the passage of the vortex may cause strong local loading changes on the blade. The vortex has a small core diameter and strength, and the blade has a small chord compared to the vortex height above the wing. In the wake vortex hazard situation, a small aircraft enters the wake generated by a large aircraft. The large aircraft produces large cored tip vortices with a high strength, which interact with the small aircraft wing, whose chord may be of the same order as the vortex core diameter and/or the vortex height. The small aircraft may undergo a strong rolling moment, creating conditions that overcome its control capability. In the case of a close-coupled canard-wing configuration, the streamwise vortex generated at the canard is convected downstream by the freestream and interacts with the wings. Since the wing has a large surface chord for the interaction to evolve, the vortex changes the pressure distribution that would exist on the wing surface if it were absent. The vortex strength and diameter, and the wing chord are larger than in the BVI case, and smaller than in the wake vortex hazard problem. This paper investigates the latter situation.

Much theoretical and experimental work has been done for the BVI and wake vortex hazard problems, where the prediction of forces and moments on the surface are of primary interest. Owing to the lengthscales involved, linear, inviscid theories of the lifting-line type yield useful results, despite the important fact that they cannot predict any detailed loading variation, such as the chordwise distribution of the surface pressure. Many investigators have used this approach (see, e.g. Smith & Lazzeroni 1960; Filotas 1971; Jones 1972; Barrows 1977; McMillan *et al.* 1978; Jung & Seath 1988). A thorough literature review of these problems can be found in Bodstein (1993).

Lifting-surface type theories have also been used, such as Silver (1966) and Hancock (1971). It is worth mentioning Hancock's work, since he obtained results similar to ours with a different approach. Hancock modelled the BVI problem for a wing of finite chord and infinite span. An integral equation was solved for the vorticity distribution in the wing, which varies with both the chordwise and the streamwise coordinates and satisfies a linearized Kutta condition at the trailing-edge. Owing to the assumptions made, his solution is valid for small chord wings. Using some simplifying assumptions based on a lifting-line type of approximation Hancock assumes a classical series solution for the vorticity distribution in the plane of the wing. A power series is identified in terms of K (defined by equation (3) below) for the series coefficients, where the first and second terms give an anti-symmetric and a symmetric loading, respectively. Hancock's theory was later compared to pressure measurements obtained by Patel & Hancock (1974) for a *low-Reynolds-number* flow. Some agreement was obtained between the data and the theory of Hancock for cases of weak interaction, although the *vortex strength was not measured* (an estimated value was used). Patel & Hancock also performed flow visualization experiments and observed that vortex breakdown and secondary separation of the wing's boundary layer occurred, for strong interaction cases.

Numerical methods have also been applied to study the BVI problem, ranging from

surface-singularity panel methods (Maskew 1983) to finite-difference algorithms for the Euler equations (Srinivasan, Chyu & Steger 1981). These results present discrepancies when compared to experimental results, owing mainly to the limitations of the numerical models (Bodstein 1993).

In addition to Patel & Hancock's experiments, other experimental results can also be found (e.g. Smith & Lazzeroni 1960; Harvey & Perry 1971; Ham 1975; McMillan *et al.* 1978; McAllister & Tung 1984; Mehta & Lim 1984; Seath & Wilson 1986). These authors performed experiments to study either the BVI or the wake vortex hazard problems, in either water or wind tunnels, but all of them studied flows with a *low Reynolds number* (based on the surface chord). In summary, they observed that the interaction does affect the loading on the wing. For strong interactions secondary separation and vortex breakdown also occur, accompanied of a large lateral vortex displacement.

The focus in this paper is on the study of the three-dimensional interaction of a streamwise vortex with a large-chord surface, which is typical of the flow around a close-coupled canard-wing configuration. When the canard and the wing have highly swept leading edges they generate vortices that co-exist on the top of the main wing (Hoeijmakers 1990). Since this flow is quite complex, we will picture here a physical situation where the wing is assumed to have a large chord and no sweep. The details of any vortex generation on the canard are of no importance, and the surface chord is large enough so that suction effects caused by the vortex on the surface are not negligible.

The objective of this study is twofold: to develop a mathematical model that captures the main loading variation on the wing surface; and to obtain experimental results that reveal the main features of the flow and the applicability of the model. Our experimental set-up covered flows with a *larger wing surface chord* and a *higher Reynolds number* than the ones found in the literature. In addition, we *measured* the *vortex strength* and *velocity profiles* in the vortex core, in contrast to previous papers on the subject. Preliminary results of our work can be found in Bodstein, George & Hui (1993).

In §2 a theoretical potential flow model based on the three-dimensional Laplace's equation is developed and solved analytically. Section 3 describes the set-up and the techniques that we used to study this flow experimentally. The theoretical and experimental results are compared in §4. Conclusions are drawn in §5.

2. Theoretical model

2.1. *Physical model*

A physical model of the problem is depicted in figure 1. Since the surface chord is considered to be very large, it is assumed that the leading-edge is far enough away from the trailing-edge such that effects caused by the leading and trailing-edges can be analysed separately, and the surface can be assumed to be semi-infinite in both cases. In this paper, only the leading-edge problem is considered. As shown in figure 1, the surface is assumed to be semi-infinite, with $0 < x < \infty$ and $-\infty < y < \infty$, and to have zero thickness. It lies in the (x, y)-plane, for $x > 0$, with zero incidence with respect to the free-stream direction. The free-stream speed, U_∞, is in the x-direction. The vortex is considered to be a straight vortex line of strength Γ, with its axis also in the free-stream direction and located at a height h above the surface centreline. The flow is three-dimensional and assumed to be steady, incompressible, inviscid and irrotational. Figure 1 also shows the Cartesian coordinate system used.

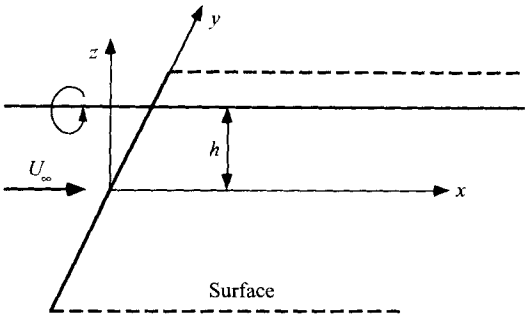

FIGURE 1. Model: a vortex of strength Γ at height h interacting with a semi-infinite surface.

A second interpretation to this formulation is also possible. One may consider this model to yield a solution to the flow in the leading-edge region of any finite chord wing, with an infinite span. In this case, our model provides an asymptotic solution for small values of x, which can, theoretically, be matched to a solution for the trailing-edge region (still not known). The first view of the problem is the one adopted here, since our experimental results were obtained for large chord wings.

2.2. *Mathematical model*

The mathematical problem for a steady, incompressible, inviscid and irrotational flow consists of solving Laplace's equation for the velocity potential ϕ subject to the impermeability condition on the surface and the condition that the velocity potential approaches the sum of the free-stream and the vortex velocity potentials at large distances away from the leading edge, in the negative x-direction. As x tends to positive infinity, the solution is expected to asymptotically approach the solution to the problem of a two-dimensional point-vortex over an infinite plane (Milne-Thompson 1955). However, this is not a boundary condition, and must be verified *a posteriori*. Normalizing all the variables by U_∞ and h, the following boundary-value problem can be set up

$$\nabla^2\phi = 0, \tag{1a}$$

$$\frac{\partial\phi}{\partial z} = 0 \quad \text{at } z = 0 \quad \text{for } x \geqslant 0, \tag{1b}$$

$$\phi \to \phi_v + \phi_\infty \quad \text{as } x^2+y^2+z^2 \to \infty \quad \text{for } x < 0, \tag{1c}$$

where ϕ_∞ is the free-stream velocity potential and ϕ_v is the vortex velocity potential, which are given by

$$\phi_\infty = x, \tag{2a}$$

$$\phi_v = K\tan^{-1}\left(\frac{z-1}{y}\right). \tag{2b}$$

The dimensionless parameter K that appears in (2b) is a measure of how strong the interaction is, and it is defined as

$$K \equiv \frac{\Gamma}{2\pi U_\infty h}. \tag{3}$$

K can be interpreted as a ratio of the transverse velocity induced by the vortex to the free-stream velocity. It should be noted that h is the only lengthscale in the problem

and, therefore, effects of Γ and h, are all lumped into the definition of K. For Γ fixed, asymptotic limiting cases where $h \to 0$ corresponds to the case where $K \to \infty$, whereas cases where $h \to \infty$ corresponds to $K \to 0$. The dependence of K on U_∞ is expected to be very weak, since classical aerodynamics arguments can be used to show that K is independent of U_∞, for a given upstream wing geometry (Bodstein 1993).

Generally speaking $|K| < 1$ in real flight. If it is assumed that K is a small parameter, so that $0 < K \ll 1$, the solution for ϕ can be expanded as an asymptotic series given by

$$\phi = \phi_0 + K\phi_1 + K^2\phi_2 + \ldots. \tag{4}$$

Substituting (4) into (1) and equating like powers of K, the following sequence of boundary-value problems can be set up

$$\nabla^2\phi_0 = 0, \tag{5a}$$

$$\frac{\partial\phi_0}{\partial z} = 0 \quad \text{at } z = 0 \quad \text{for } x \geqslant 0, \tag{5b}$$

$$\phi_0 \to \phi_\infty \quad \text{as } x^2+y^2+z^2 \to \infty \quad \text{for } x < 0, \tag{5c}$$

$$\nabla^2\phi_1 = 0, \tag{6a}$$

$$\frac{\partial\phi_1}{\partial z} = 0 \quad \text{at } z = 0 \quad \text{for } x \geqslant 0, \tag{6b}$$

$$\phi_1 \to \phi_v \quad \text{as } x^2+y^2+z^2 \to \infty \quad \text{for } x < 0, \tag{6c}$$

$$\vdots$$

$$\nabla^2\phi_n = 0, \tag{7a}$$

$$\frac{\partial\phi_n}{\partial z} = 0 \quad \text{at } z = 0 \quad \text{for } x \geqslant 0, \tag{7b}$$

$$\phi_n \to 0 \quad \text{as } x^2+y^2+z^2 \to \infty \quad \text{for } x < 0, \tag{7c}$$

where $n \geqslant 2$. The solution to (5) is $\phi_0 = x$, that is, a uniform flow. Because the solution of the boundary-value problem (7) must be unique, only the trivial solution $\phi_n = 0$ is admitted. Any eigensolution (sources, dipoles, etc.) placed on the (x, y)-plane does satisfy (7*a*) and (7*c*), but it does not satisfy the boundary condition (7*b*) since it blows up at the point where the singularity is placed. Singularities placed in the fluid region do not satisfy Laplace's equation at their positions, and, therefore, all eigensolutions must be discarded. These results imply that the series (4) terminates at $n = 1$, which produces an exact solution for ϕ given by

$$\phi = x + K\phi_1. \tag{8}$$

Equation (8) also implies that, from a purely mathematical point of view, we can relax the initial assumption that K is a small parameter, since the original problem can now be viewed as a superposition of solutions, that is, a sum of a uniform flow and a flow due to the vortex. Any restriction on how large K can be must be supported by a physical argument. For large values of K the flow separates on the surface, and the whole model breaks down.

Turning our attention back to the boundary-value problem (6) we recognize that ϕ_v is a solution to Laplace's equation, which allows us to define a perturbation velocity potential, φ, according to

$$\varphi \equiv \phi_1 - \phi_v. \tag{9}$$

With this filtering procedure equations (6) can be written as

$$\frac{\partial^2 \varphi}{\partial x^2}+\frac{\partial^2 \varphi}{\partial y^2}+\frac{\partial^2 \varphi}{\partial z^2}=0, \tag{10a}$$

$$\frac{\partial \varphi}{\partial z}=-\frac{y}{1+y^2} \quad \text{at } z=0 \quad \text{for } x \geqslant 0, \tag{10b}$$

$$\varphi \to 0 \quad \text{as } x^2+y^2+z^2 \to \infty \quad \text{for } x<0. \tag{10c}$$

The boundary-value problem (10) can be solved using the Fourier transform applied to x and y, and the Wiener–Hopf technique, since the boundary condition (10b) is valid only for positive values of x. The perturbation velocity potential φ is required to have continuous second derivatives everywhere in the fluid region, except along the vortex line. Taking the Fourier transform of (10) with respect to y yields

$$\frac{\partial^2 \tilde{\varphi}}{\partial x^2}+\frac{\partial^2 \tilde{\varphi}}{\partial z^2}-\lambda^2 \tilde{\varphi}=0, \tag{11a}$$

$$\frac{\partial \tilde{\varphi}}{\partial z}=-\mathrm{i}\pi \operatorname{sgn}(\lambda)\mathrm{e}^{-|\lambda|} \equiv g(\lambda) \quad \text{at } z=0 \quad \text{for } x \geqslant 0, \tag{11b}$$

$$\tilde{\varphi} \to 0 \quad \text{as } x^2+y^2+z^2 \to \infty \quad \text{for } x<0, \tag{11c}$$

where $\tilde{\varphi}$ is the Fourier transform of φ, defined as

$$\tilde{\varphi}(x, \lambda, z) \equiv \int_{-\infty}^{\infty} \varphi(x, y, z)\mathrm{e}^{-\mathrm{i}\lambda y}\,\mathrm{d}y.$$

The Fourier transform with respect to x reduces (11) to

$$\frac{\mathrm{d}^2 \Phi}{\mathrm{d}z^2}-(\omega^2+\lambda^2)\Phi=0, \tag{12a}$$

$$\frac{\mathrm{d}\Phi}{\mathrm{d}z}=H(\omega, \lambda) \quad \text{at } z=0 \quad \text{for } x \geqslant 0, \tag{12b}$$

$$\Phi \to 0 \quad \text{as } x^2+y^2+z^2 \to \infty \quad \text{for } x<0, \tag{12c}$$

which has the following solution

$$\Phi(\omega, \lambda, z)=-\operatorname{sgn}(z)\frac{H(\omega, \lambda)}{(\omega^2+\lambda^2)^{1/2}}\exp\left(-|z|(\omega^2+\lambda^2)^{1/2}\right). \tag{13}$$

The function Φ is the Fourier transform of $\tilde{\varphi}$ with respect to x, defined analogously as above. The boundary condition $H(\omega, \lambda)$ can be determined using the Wiener–Hopf technique (Nobel 1958). Thus, evaluating (12b), we can write

$$\frac{\mathrm{d}\Phi}{\mathrm{d}z}(\omega, \lambda, z=0)=\int_{-\infty}^{0}\frac{\partial \tilde{\varphi}}{\partial z}(x, \lambda, z=0)\mathrm{e}^{-\mathrm{i}\omega x}\,\mathrm{d}x + \int_{0}^{\infty}\frac{\partial \tilde{\varphi}}{\partial z}(x, \lambda, z=0)\mathrm{e}^{-\mathrm{i}\omega x}\,\mathrm{d}x = H(\omega, \lambda). \tag{14}$$

The integral defined for $x > 0$ converges only for $\mathrm{Im}[\omega] < 0$, producing a function that is analytic in some lower-half ω-plane. Conversely, the integral defined for $x < 0$ converges only where $\mathrm{Im}[\omega] > 0$, generating a function $W_+(\omega, \lambda)$ that is analytic in some upper-half ω-plane. Since its integrand is unknown, $W_+(\omega, \lambda)$ must be determined as part of the solution. With (11*b*), equation (14) becomes

$$\frac{\mathrm{d}\Phi}{\mathrm{d}z}(\omega, \lambda, z = 0) = W_+(\omega, \lambda) + g(\lambda)\left[\frac{1}{\mathrm{i}(\omega - \mathrm{i}\epsilon)}\right]_- = H(\omega, \lambda), \tag{15}$$

where the ' + ' and ' − ' subscripts denote that the function is analytic in some upper- and lower-half ω-planes, respectively. These domains of analyticity will be determined below. The function in square brackets is the Fourier transform of the unit step function, which exists only if defined in some lower-half ω-plane. This is consistent with the introduction of ϵ, for $0 < \epsilon \ll 1$, which displaces the pole from the real axis to the upper-half plane of ω and includes the real axis in the Wiener–Hopf strip of analyticity where the inversion process must be performed (Carrier, Krook & Pearson 1983). The limit as $\epsilon \to 0$ must be taken after the inversion procedure is completed.

From physical grounds we expect $\Phi(\omega, \lambda, z)$ to be continuous at $z = 0$, for $x < 0$, and discontinuous at $z = 0$, for $x > 0$, since the surface is modelled as a vortex sheet in the flow. Mathematically, the surface must be a branch cut in the domain. Indeed, it can be inferred from (13) that the jump in $\Phi(\omega, \lambda, z)$ across the plane $z = 0$, for $x < 0$, is zero, and the jump in $\Phi(\omega, \lambda, z)$, for $x > 0$, is given by

$$\Delta\Phi = \Phi(\omega, \lambda, z = 0^+) - \Phi(\omega, \lambda, z = 0^-) = -2\frac{H(\omega, \lambda)}{(\omega^2 + \lambda^2)^{1/2}} \equiv F_-(\omega, \lambda). \tag{16}$$

This equation defines a function $F_-(\omega, \lambda)$, which is analytic in some lower-half ω-plane. Equation (16) can, now, be substituted into (15) to produce a Wiener–Hopf equation in ω,

$$F_-(\omega, \lambda) = \frac{-2}{(\omega^2 + \lambda^2)^{1/2}}\left\{g(\lambda)\left[\frac{1}{\mathrm{i}(\omega - \mathrm{i}\epsilon)}\right]_- + W_+(\omega, \lambda)\right\}. \tag{17}$$

The equation above has a pole at $\mathrm{i}\epsilon$ and two branch points, at $\mathrm{i}\lambda$ and $-\mathrm{i}\lambda$. The Fourier transform variable λ can be positive or negative and the Wiener–Hopf equation turns out to have the same form if λ is replaced by $|\lambda|$ in (17). So, the square-root term in the equation above can be written as $((\omega - \mathrm{i}|\lambda|)(\omega + \mathrm{i}|\lambda|))^{1/2}$, and the branch cuts must be chosen such that $\mathrm{Re}[((\omega - \mathrm{i}|\lambda|)(\omega + \mathrm{i}|\lambda|))^{1/2}] > 0$, which is the condition for the convergence at infinity of the exponential term in the solution (13). The branch cuts extend from $\pm\mathrm{i}|\lambda|$ to $\pm\mathrm{i}\infty$, respectively. Noting that this square-root term is a product of a ' + ' and a ' − ' function, the Wiener–Hopf equation can be rearranged as follows

$$-\frac{1}{2g(\lambda)}[(\omega - \mathrm{i}|\lambda|)^{1/2}]_- F_-(\omega, \lambda) = \left[\frac{1}{\mathrm{i}(\omega - \mathrm{i}\epsilon)}\right]_-\left[\frac{1}{(\omega + \mathrm{i}|\lambda|)^{1/2}}\right]_+ + \frac{W_+(\omega, \lambda)}{g(\lambda)}\left[\frac{1}{(\omega + \mathrm{i}|\lambda|)^{1/2}}\right]_+. \tag{18}$$

In equation (18), the left-hand side is analytic in some lower-half ω-plane, whereas the second term on the right-hand side is analytic in some upper-half ω-plane. The remaining term is analytic in the strip of analyticity between the pole at $\mathrm{i}\epsilon$ and the

branch point at $-\mathrm{i}|\lambda|$. Thus, it can be split into a sum of a '+' and a '−' function, so that the Wiener–Hopf equation becomes

$$-\frac{1}{2g(\lambda)}[(\omega-\mathrm{i}|\lambda|)^{1/2}]_- F(\omega,\lambda)-M_-(w,\lambda)$$

$$= M_+(\omega,\lambda)+\frac{W_+(\omega,\lambda)}{g(\lambda)}\left[\frac{1}{(\omega+\mathrm{i}|\lambda|)^{1/2}}\right]_+ = E(\omega,\lambda), \quad (19)$$

where $M_+(\omega,\lambda)$ and $M_-(\omega,\lambda)$ are given by

$$M_+(\omega,\lambda) = \frac{1}{\mathrm{i}(\omega-\mathrm{i}\epsilon)(\omega+\mathrm{i}|\lambda|)^{1/2}} - \frac{1}{\mathrm{i}(\omega-\mathrm{i}\epsilon)(\mathrm{i}\epsilon+\mathrm{i}|\lambda|)^{1/2}}, \quad (20a)$$

$$M_-(\omega,\lambda) = \frac{1}{\mathrm{i}(\omega-\mathrm{i}\epsilon)(\mathrm{i}\epsilon+\mathrm{i}|\lambda|)^{1/2}}. \quad (20b)$$

The term on the left-hand side of (19) is the analytic continuation of the term on the right-hand side (and vice versa), and together they define an entire function $E(\omega,\lambda)$. In order to determine $E(\omega,\lambda)$, a Wiener–Hopf argument must be used, that is, the behaviour of the two sides of (19) near the leading edge must be examined. In the complex ω-plane the behaviour of $W_+(\omega,\lambda)$ and $F_-(\omega,\lambda)$ near the leading edge are determined by their behaviour as $\omega\to\infty$. At $x=0$ we expect a singularity to exist in the vertical component of the perturbation velocity field. Since this singularity in thin wing theory is a square-root singularity we assume the same to occur here. Thus, if $\tilde{\varphi}_z(x,\lambda,z=0)$ behaves as $1/x^{1/2}$ as the leading edge is approached from the left, it is integrable there, and $W_+(\omega,\lambda)\sim 1/\omega^{1/2}$ as $\omega\to\infty$. Consequently, $W_+(\omega,\lambda)\to 0$ as $|\omega|\to\infty$, in the region $\mathrm{Im}[\omega]>-|\lambda|$. By the same reasoning, a square-root singularity should also occur in the x-component of the perturbation velocity field. If this assumption is true, we anticipate that $\tilde{\varphi}(x,\lambda,z=0)\sim x^{1/2}$ near the leading edge, and, therefore, it is bounded at $x=0$. For this reason, $F_-(\omega,\lambda)\sim 1/\omega^{3/2}$ at the leading edge and $\omega F_-(\omega,\lambda)$ is integrable as $|\omega|\to\infty$, in the region $\mathrm{Im}[\omega]<\epsilon$. So, $F_-(\omega,\lambda)\to 0$ as $|\omega|\to\infty$, and each side of (19) tends to zero as $|\omega|\to\infty$ in its domain of definition. Using Liouville's theorem (Carrier *et al.* 1983), $E(\omega,\lambda)$ must be identically zero, and $F_-(\omega,\lambda)$ and $W_+(\omega,\lambda)$ are found to be

$$F_-(\omega,\lambda) = -2g(\lambda)\frac{M_-(\omega,\lambda)}{(\omega-\mathrm{i}|\lambda|)^{1/2}}, \quad W_+(\omega,\lambda) = -M_+(\omega,\lambda)g(\lambda)(\omega+\mathrm{i}|\lambda|)^{1/2}, \quad (21a,b)$$

with $M_+(\omega,\lambda)$ and $M_-(\omega,\lambda)$ given by (20). From (21) it can be seen that the lower-half plane of analyticity of $F_-(\omega,\lambda)$ is $\mathrm{Im}[\omega]<\epsilon$, and the upper-half plane of analyticity of $W_+(\omega,\lambda)$ is $\mathrm{Im}[\omega]>-|\lambda|$. The overlapping region defines the strip of analyticity where the inversion process in the ω-plane must be performed. Equations (21) also indicate that the asymptotic behaviour of $F_-(\omega,\lambda)$ and $W_+(\omega,\lambda)$, as $\omega\to\infty$, are correct.

Substituting (21*b*) into (15), or (21*a*) into (16), the boundary condition $H(\omega,\lambda)$ can be obtained. Using this result in (13), the solution in the two-dimensional Fourier space (ω,λ) is

$$\Phi(\omega,\lambda,z) = \pi\,\mathrm{sgn}(z)\,\mathrm{sgn}(\lambda)\frac{\exp(-|\lambda|)}{(\mathrm{i}\epsilon+\mathrm{i}|\lambda|)^{1/2}}\frac{\exp(-|z|(\omega^2+\lambda^2)^{1/2})}{(\omega-\mathrm{i}\epsilon)(\omega-\mathrm{i}|\lambda|)^{1/2}}, \quad (22)$$

where the definition of $g(\lambda)$, equation (11*b*), was used in (22).

From the Fourier inversion formula, the solution in the physical space can be written as

$$\varphi(x,y,z) = -\frac{1}{4\pi}\operatorname{sgn}(z)\int_{-\infty}^{\infty}\frac{\operatorname{sgn}(\lambda)\exp(-|\lambda|)}{(i\epsilon+i|\lambda|)^{1/2}}\exp(i\lambda y)\int_{-\infty}^{\infty}\frac{\exp(-|z|(\omega^2+\lambda^2)^{1/2})}{(\omega-i\epsilon)(\omega-i|\lambda|)^{1/2}} \times \exp(i\omega x)\,d\omega\,d\lambda. \quad (23)$$

Performing a contour integration on the innermost integral of (23) along the real axis in the ω-plane, expanding the outermost integral, and taking the limit as $\epsilon \to 0$, we obtain

$$\varphi(x,y,z) = \frac{1}{\pi}\operatorname{sgn}(z)\left[\pi\tan^{-1}\left(\frac{y}{1+|z|}\right) - \int_0^{\infty}\frac{\sin(\lambda y)\,e^{-\lambda}}{\lambda^{1/2}}\int_{\lambda}^{\infty}\frac{\cos(|z|(\eta^2-\lambda^2)^{1/2})}{\eta(\eta-\lambda)^{1/2}}e^{-\eta x}\,d\eta\,d\lambda\right] \quad \text{for } x \geqslant 0, \quad (24a)$$

$$\varphi(x,y,z) = \frac{1}{\pi}\operatorname{sgn}(z)\int_0^{\infty}\frac{\sin(\lambda y)\,e^{-\lambda}}{\lambda^{1/2}} \times \int_{\lambda}^{\infty}\frac{\sin(|z|(\eta^2-\lambda^2)^{1/2})}{\eta(\eta+\lambda)^{1/2}}e^{\eta x}\,d\eta\,d\lambda \quad \text{for } x < 0. \quad (24b)$$

Equations (24) comprise the solution to the boundary-value problem (10). In particular, on the plane $z = 0$, equations (24) can be integrated analytically to give the perturbation velocity potential on the surface

$$\varphi(x,y,z=0) = \begin{cases} \operatorname{sgn}(z)\operatorname{Im}\left[\ln\left(\dfrac{(1+x+iy)^{1/2}-x^{1/2}}{(1+x+iy)^{1/2}+x^{1/2}}\right)\right] & \text{for } x \geqslant 0. \\ 0 \quad \text{for } x < 0 \end{cases} \quad (25)$$

Equation (25) shows that the surface is indeed a branch cut in the domain of definition of $\varphi(x,y,z)$. An asymptotic expansion of (25), for small values of x, indicates that the assumption of boundedness of $\varphi(x,y,z=0)$, as $x \to 0$, is correct.

2.3. *Velocity and pressure fields on the surface*

Analysis of the velocity field brings up some interesting aspects of the solution. The perturbation velocity components in the (x,y)-plane, for $x > 0$, calculated from (25), are

$$\frac{\partial\varphi}{\partial x}(x,y,z=0) = -\operatorname{sgn}(z)\,x^{-1/2}\operatorname{Im}\left[\frac{1}{(1+x+iy)^{1/2}}\right] \quad \text{for } x > 0, \quad (26a)$$

$$\frac{\partial\varphi}{\partial y}(x,y,z=0) = \operatorname{sgn}(z)\,x^{1/2}\operatorname{Im}\left[\frac{i}{(1+iy)(1+x+iy)^{1/2}}\right] \quad \text{for } x > 0. \quad (26b)$$

Equations (26) can be used to interpret our solution as a continuous distribution of horseshoe vortices placed on the surface. In this case the bound and trailing vortices, respectively, are

$$\gamma_y \equiv \frac{\partial\varphi}{\partial x}(x,y,z=0^+) - \frac{\partial\varphi}{\partial x}(x,y,z=0^-) = -\frac{2}{x^{1/2}}\operatorname{Im}\left[\frac{1}{(1+x+iy)^{1/2}}\right],$$

$$\gamma_x \equiv \frac{\partial\varphi}{\partial y}(x,y,z=0^+) - \frac{\partial\varphi}{\partial y}(x,y,z=0^-) = 2x^{1/2}\operatorname{Im}\left[\frac{i}{(1+iy)(1+x+iy)^{1/2}}\right].$$

The perturbation velocity components for $x < 0$ are obtained from the general solution for q, equation (24*b*). Taking the derivative with respect to x, y and z, and setting $z = 0$, yields

$$\frac{\partial \varphi}{\partial x}(x, y, z = 0) = \frac{\partial \varphi}{\partial y}(x, y, z = 0) = 0 \quad \text{for } x < 0, \tag{27a, b}$$

$$\frac{\partial \varphi}{\partial z}(x, y, z = 0) = -\frac{y}{1+y^2} - \frac{1}{|x|^{1/2}} \operatorname{Im}\left[\frac{(1+|x|+\mathrm{i}y)^{1/2}}{1+\mathrm{i}y}\right] \quad \text{for } x < 0. \tag{27c}$$

Equations (27*a*) and (27*b*) show a remarkable result: the x- and y-velocity components in the plane $z = 0$, for $x < 0$, are zero. The first term in (27*c*) corresponds to the velocity induced by the vortex, whereas the second has a square-root singularity at the leading edge.

Performing an asymptotic analysis of the velocity components above, more information on the solution can be obtained. First, expanding equations (26) for small values of x yields

$$\frac{\partial \varphi}{\partial x}(x, y, z = 0) \sim -\operatorname{sgn}(z) \frac{1}{x^{1/2}} \operatorname{Im}\left[\frac{1}{(1+\mathrm{i}y)^{1/2}}\right] \quad \text{as } x \to 0^+, \tag{28a}$$

$$\frac{\partial \varphi}{\partial y}(x, y, z = 0) \sim -\operatorname{sgn}(z) x^{1/2} \operatorname{Im}\left[\frac{\mathrm{i}}{(1+\mathrm{i}y)^{3/2}}\right] \quad \text{as } x \to 0^+. \tag{28b}$$

Equations (28) show that, as $x \to 0^+$, the perturbation velocity component in the x-direction is anti-symmetric in y and has the expected square-root singularity at $x = 0$. On the other hand, the component in the y-direction is symmetric in y and is continuous at $x = 0$. The component in the z-direction, as x approaches zero from the left, can be obtained from (27*c*),

$$\frac{\partial \varphi}{\partial z}(x, y, z = 0) \sim -\frac{1}{|x|^{1/2}} \operatorname{Im}\left[\frac{1}{(1+\mathrm{i}y)^{1/2}}\right] \quad \text{as } x \to 0^-, \tag{29}$$

which indicates the existence of an integrable square-root singularity at $x = 0$. This again confirms the integrability assumption of φ_z at the surface's leading-edge used in the Wiener–Hopf argument. In addition, (29) shows an anti-symmetric behaviour of $\varphi_z(x, y, z = 0)$ with respect to y, basically owing to the vortex downwash.

The behaviour of the perturbation velocity components as $x \to \infty$ is also of interest. Expanding (26) for large values of x yields

$$\frac{\partial \varphi}{\partial x}(x, y, z = 0) \sim \tfrac{1}{2}\operatorname{sgn}(z) \frac{y}{x^2} \quad \text{as } x \to \infty, \tag{30a}$$

$$\frac{\partial \varphi}{\partial y}(x, y, z = 0) \sim -\operatorname{sgn}(z) \frac{1}{1+y^2} \quad \text{as } x \to \infty. \tag{30b}$$

Equation (30*a*) shows that the x-component decays very fast at infinity, and just U_∞ remains. Furthermore, using (30*b*) and the boundary condition (10*b*), the total velocity components on the top of the surface in the y- and z-directions converge to

$$v(x, y, z = 0^+) \equiv \frac{\partial \phi}{\partial y}(x, y, z = 0^+) \sim 2K \frac{1}{1+y^2} \quad \text{as } x \to \infty, \tag{31a}$$

$$w(x, y, z = 0^+) \equiv \frac{\partial \phi}{\partial z}(x, y, z = 0^+) = 0 \quad \text{as } x \to \infty. \tag{31b}$$

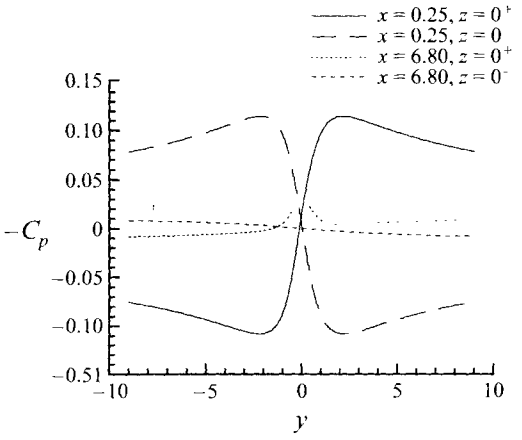

FIGURE 2. $-C_p$ on the top and bottom of the surface for $K = 0.089$.

Equations (31) constitute the solution to the two-dimensional point-vortex/infinite-plane problem (Milne-Thompson 1955), showing that our solution is asymptotically correct. As $x \to -\infty$, the perturbation velocity component in the z-direction tends to zero at a rate of the order of $|x|^{-2}$, which is expected because just the vortex velocity potential remains non-zero far upstream of the leading edge.

The pressure distribution is obtained from Bernoulli's equation, written as

$$-C_p = 2K\frac{\partial q'}{\partial x} + K^2\left[\left(\frac{\partial q'}{\partial x}\right)^2 + \left(\frac{\partial \phi_y}{\partial y} + \frac{\partial q'}{\partial y}\right)^2\right], \tag{32}$$

where

$$C_p \equiv \frac{p - p_\infty}{\frac{1}{2}\rho U_\infty^2}.$$

The perturbation velocity components on the surface are given by equations (26), and ϕ_v from (2*b*). Typical graphs of the pressure distributions on the top and bottom of the surface are shown in figure 2, for $K = 0.089$. This value of K is encountered in real flight for weak interactions, and was used in our experiments. First, we consider $-C_p$ at a chordwise station near the leading edge of the surface. Both distributions possess an anti-symmetric behaviour with respect to the spanwise coordinate, which is due to the vortex downwash. On the top surface the flow hits the surface on one side of the vortex and increases the pressure, whereas, on the other side, the flow moves away from the surface, decreasing the pressure. The opposite effect occurs on the bottom surface. The pressure distributions at a chordwise station far downstream from the leading edge are also shown in figure 2. It shows an approximately symmetric behaviour on the top surface and an anti-symmetric behaviour on the bottom surface. On the top, the vortex generates a suction peak, since the fluid rotating around the vortex is accelerated to pass in the gap between the vortex and the impermeable surface, decreasing the pressure. Beyond the line just underneath the vortex, the flow decelerates, increasing the pressure again. In this region, the flow is locally two-dimensional. This suction effect is responsible for the generation of lift due entirely to the vortex. On the bottom surface the fluid starts to 'forget' the existence of the vortex as the flow progresses downstream, and the anti-symmetric effect present near the leading-edge still persists, although decaying rapidly. The symmetric and anti-symmetric components of the pressure distribution were also obtained by Hancock (1971), in his model of the flow around a helicopter blade.

The asymptotic expansions for the velocity components can be used in (32). For large values of x, equations (30) yield

$$-C_p \sim 2K^2\frac{(1+\mathrm{sgn}(z))}{(1+y^2)^2} - K\,\mathrm{sgn}(z)\frac{y}{x^2} \quad \text{as } x \to \infty \tag{33}$$

for the first two terms. On the top of the surface the first term of (33) dominates. The pressure distribution in this case is symmetric in y and proportional to K^2. On the bottom of the surface, the first term vanishes and the second term dominates, which is proportional to K and anti-symmetric in y, as shown in figure 2. For small values of x, the pressure coefficient behaves as

$$-C_p \sim \frac{K^2}{x}\left(\mathrm{Im}\left[\frac{1}{(1+\mathrm{i}y)^{1/2}}\right]\right)^2 - 2K\,\mathrm{sgn}(z)\frac{1}{x^{1/2}}\mathrm{Im}\left[\frac{1}{(1+\mathrm{i}y)^{1/2}}\right] \quad \text{as } x \to 0^+. \tag{34}$$

The first term on the right-hand side of (34) has a non-integrable singularity at $x = 0$ and is proportional to K^2. The second term is proportional to K and has an integrable square-root singularity at $x = 0$. In regions near (but not very close to) the leading edge, the second term in (34) will dominate, and the pressure distribution becomes anti-symmetric in y and proportional to K, as shown in figure 2. However, in regions very close to the leading edge, the first term is dominant. In a real flow, under moderate flight conditions, usually $|K| < 1$. Since the first term in (34) is proportional to K^2, it will be important only for very small values of x, where the adverse pressure gradient in the x-direction imposed by this first term behaves as x^{-2}. In this narrow region ($0 < x \ll 1$), this pressure gradient is likely to cause a local separation bubble to occur near the leading edge, and the present model is no longer valid. If K is very large, the entire model is likely to break down owing to three-dimensional boundary-layer separation on the surface. This region, where this singular term is important, is strongly dominated by viscosity. Separation at the leading edge is observed to occur in our experiments (§4). Furthermore, the assumption that the leading edge is sharp is, in fact, a major source of difficulties. Theoretically, it should be possible to remove this singular behaviour by adding a round nose to the surface. The same type of singularity was observed to occur in thin airfoil theory, where spurious singularities arise at stagnation points (Van Dyke 1956). A first-order solution in an asymptotic expansion in terms of a thickness parameter presents a square-root singularity at the leading edge, whereas a second-order solution shows the appearance of a $1/x$-type of singularity at the same point. The problem was resolved by straining the coordinates near the edge, and matching it with the thin airfoil theory solution (see also Van Dyke 1975). A last point on this issue is the fact that a non-integrable singularity of this type implies that an infinite force will act on the surface. However, it should be noted that if C_p integrates to an infinite force on the top of the surface, it also integrates to an infinite force on the bottom of the surface. Thus, there is no net contribution to ΔC_p, the pressure coefficient differential, defined as $\Delta C_p \equiv C_p^- - C_p^+$. In fact, from (32), ΔC_p is given by

$$\Delta C_p(x,y) = -4K\frac{1}{x^{1/2}}\mathrm{Im}\left[\frac{1}{(1+x+\mathrm{i}y)^{1/2}}\right] + 4K^2x^{1/2}\mathrm{Im}\left[\frac{\mathrm{i}}{(1+\mathrm{i}y)(1+x+\mathrm{i}y)^{1/2}}\right]\frac{1}{(1+y^2)}. \tag{35}$$

It follows that the behaviour of ΔC_p near the leading edge is proportional to K, anti-symmetric in y, and has an integrable square-root singularity near the leading edge.

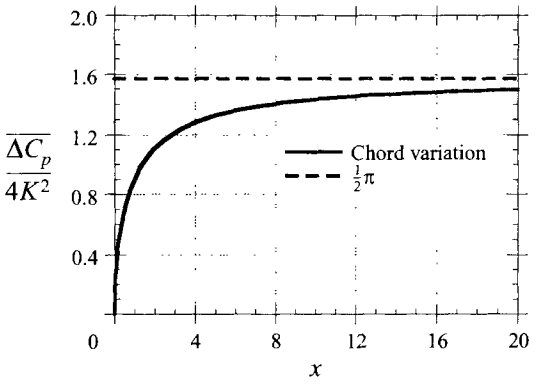

FIGURE 3. Variation of the pressure coefficient differential per unit chord along the chordwise direction.

This loading generates bending and rolling moments on the surface. Far downstream from the leading edge (as $x \to \infty$) ΔC_p is symmetric in y and is proportional to K^2, which indicates that the higher the value of K, the larger the vortex-induced lift coefficient will be.

Equation (35) can be integrated in the spanwise coordinate to give the pressure coefficient differential (or lift coefficient) per unit chord, $\overline{\Delta C_p}(x)$, owing to the interaction with the vortex. The first term of (35) vanishes because of its anti-symmetry in y, and just the second term contributes. Integrating numerically, this term yields the curve shown in figure 3. As $x \to \infty$, the value of $\overline{\Delta C_p}(x)/4K^2$ tends asymptotically to $\frac{1}{2}\pi$. Thus, $\overline{\Delta C_p}(x) \sim 2\pi K^2$, as $x \to \infty$, which can be considered an upper bound to the amount of lift per unit chord obtained.

The presence of a trailing-edge on a finite-chord wing implies that the Kutta condition must be satisfied. In other words, the pressure field must be continuous across the trailing edge. This condition requires that ΔC_p is zero at the trailing edge. Therefore, $\overline{\Delta C_p}(x)/4K^2$ must reach a maximum on the wing surface, which cannot be greater than $\frac{1}{2}\pi$, and decay to zero at the trailing edge. Hancock's model captured this behaviour. However, the values of C_p^+ and C_p^- at the trailing edge do not need to be necessarily zero. In fact, they can even present a spanwise variation, as long as they are equal. Their values depend on the trailing-edge geometry. A solution for the trailing-edge region analogous to this one for the leading-edge region is still to be obtained.

In summary, this model reveals the asymptotic structure of the pressure distribution over most of the surface of a large-chord wing owing to its interaction with a streamwise vortex. Two of its applicabilities can be point out. First, the solution obtained here can be used to calculate the three-dimensional flow in the boundary layer of the wing, and its associated topology. Secondly, the potential flow solution itself shows that the associated increase in lift on the wing owing to the vortex depends on the square of K. This solution can theoretically be matched, via the method of asymptotic expansion, to an analogous solution to the trailing-edge region, which is not known. The matched solution will, in principle, provide the best potential flow solution to the problem. The analytical or numerical solutions obtained by Silver (1967), Maskew (1983) and the others mentioned in the introduction are all based on a distribution of surface singularities, and they are potential flow solutions such as the one presented here. However, they were applied to helicopter blades, and did not captured the K^2-term. For helicopters and for the wake hazard problem the K-term is the one that generates bending or rolling moments on the wing, which are the main

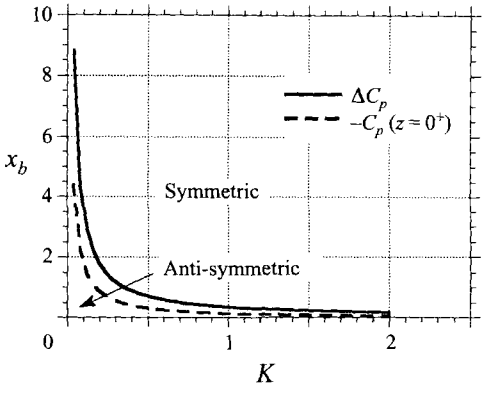

FIGURE 4. Boundary between the symmetric and anti-symmetric pressure distributions.

loads. Nevertheless, for a close-coupled canard-wing configuration, the flow feature of main interest is the extra lift caused by the vortex. Only Hancock (1971) found both terms, but his solution presents some simplifying assumptions well-suited for helicopter blades.

2.4. *Boundary between symmetric and anti-symmetric effects*

A question that arises from the pressure distribution behaviour is where the boundary between symmetric and anti-symmetric effects is. Here, this boundary will arbitrarily be defined as the position on the surface along the chordwise direction where the maximum value of the anti-symmetric effect with respect to the spanwise coordinate is equal to the maximum of the symmetric effect. In other words, a solution $x_b(K)$ is sought to the equation

$$A_{max}(K, x, y_{max}(x)) = S_{max}(K, x, y_{max}(x)), \tag{36}$$

where $y_{max}(x)$ is the point where each function has a maximum (in absolute value), and A_{max} and S_{max} are the maximum values of the anti-symmetric and the symmetric distributions, respectively.

From (35) for the pressure coefficient differential, the maximum for the first term (anti-symmetric) occurs at $y_{max}(x) = \sqrt{3}(1+x)$, and the maximum for the second term (symmetric) occurs at $y_{max}(x) = 0$. Hence, calculating the maximum values of each function and equating them, an equation of the type of (36) is obtained, which has the following solution

$$x_b = \frac{1}{2\sqrt{2}}\frac{1}{K}. \tag{37}$$

For the pressure coefficient on the top of the surface the same procedure is used. However, the term $(\partial\varphi/\partial x)^2$ in (32) was neglected based on the same argument used before to analyse (34). The equation obtained is a second-order algebraic equation in x_b, and its solution is

$$x_b = \frac{1}{16}\left[\left(-2\sqrt{2}K - 8 + \frac{\sqrt{2}}{K}\right) + \frac{1}{K}(8K^4 + 32\sqrt{2}K^3 + 56K^2 + 16\sqrt{2}K + 2)^{1/2}\right]. \tag{38}$$

Equations (37) and (38) are plotted in figure 4. They provide an approximation for the chordwise position where a smooth transition from an anti-symmetric loading changes into a symmetric one on the surface of a large-chord wing. This boundary is important because the characteristics of the pressure gradient on the surface are different in these two regions, which has implications on the boundary-layer topology

on the wing surface. The symmetric loading, for example, determines whether spanwise separation and second vortex formation are expected to occur. A finite-chord wing will have the boundary between these two types of loading moved upstream, for a fixed value of K, since the pressure field will change in a region near the trailing edge (as discussed in the previous section).

2.5. *Vortex path*

So far the vortex has been assumed to be a straight vortex filament. In the real flow the vortex is expected to curve owing to the presence of the wing surface nearby. This effect can be interpreted in ways. We can regard the wing surface as a vortex sheet. In this case the bound and trailing vortices induce a velocity field on the original vortex that displaces it in order for the vortex to follow a streamline of the flow. We can also interpret this displacement effect as being generated by an 'image vortex' situated below the surface, such that the impermeability boundary condition is satisfied on the surface. Either way, induced velocities in the free-stream direction will tend to stretch the vortex filament, whereas sidewash and downwash velocities will tilt the vortex with respect to the free-stream direction. The stretching effect is not accounted for in this analysis because the vortex is modelled as a filament.

The vortex path can be estimated by ensuring that the vortex follows a streamline. The lateral and vertical displacements are calculated upon integration along the vortex line (the x-direction) of the equations that define a family of streamlines, which yields

$$y_{iv} = y_{v_0} + \int_{-\infty}^{x} \frac{\partial \varphi}{\partial y}(\xi, y, z)|_{v_0}\, \mathrm{d}\xi, \tag{39a}$$

$$z_{iv} = z_{v_0} + \int_{-\infty}^{x} \frac{\partial \varphi}{\partial z}(\xi, y, z)|_{v_0}\, \mathrm{d}\xi. \tag{39b}$$

In (39) 'iv' denotes induced at the vortex location and 'v_0' denotes evaluation at the vortex initial position, i.e. $(x, y_{v_0} = 0, z_{v_0} = 1)$. The integrands of (39), evaluated from (24), are

$$y_{iv} = \begin{cases} y_{iv_n}(x, y_{v_0} = 0, z_{v_0} = 1) & \text{for } x < 0, \\ y_{iv_n}(x = 0, y_{v_0} = 0, z_{v_0} = 1) + \frac{1}{2}Kx + y_{iv_p}(x, y_{v_0} = 0, z_{v_0} = 1) & \text{for } x > 0, \end{cases} \tag{40a}$$

where

$$z_{iv} = z_{v_0} + 0 = 1, \tag{40b}$$

$$y_{iv_n}(x, y_{v_0} = 0, z_{v_0} = 1) \equiv \frac{K}{\pi} \int_0^\infty \lambda^{1/2} \mathrm{e}^{-\lambda} \int_\lambda^\infty \frac{\sin(\eta^2 - \lambda^2)^{1/2}}{\eta^2(\eta + \lambda)^{1/2}} \mathrm{e}^{\eta x}\, \mathrm{d}\eta\, \mathrm{d}\lambda, \tag{41a}$$

$$y_{iv_p}(x, y_{v_0} = 0, z_{v_0} = 1) \equiv -\frac{K}{\pi} \int_0^\infty \lambda^{1/2} \mathrm{e}^{-\lambda} \int_\lambda^\infty \frac{\cos(\eta^2 - \lambda^2)^{1/2}}{\eta^2(\eta - \lambda)^{1/2}} (1 - \mathrm{e}^{-\eta x})\, \mathrm{d}\eta\, \mathrm{d}\lambda. \tag{41b}$$

Equations (41) were integrated numerically using the subroutines of Press *et al.* (1989). The lateral vortex displacement is shown in figure 5, for $K = 0.089$. It can be seen that the vortex curves only in a region near the leading edge, and, as $x \to -\infty$, the presence of the plate is not felt by the vortex. Downstream from the leading edge only the 'two-dimensional image effect' survives, and the vortex follows approximately a straight line with slope $\frac{1}{2}K$ (see equation (40a)). Equation (40b) indicates that the vertical vortex displacement is zero, to the degree of approximation used here, and it remains at its original height above the surface.

This calculation was performed assuming that the original vortex path is a straight

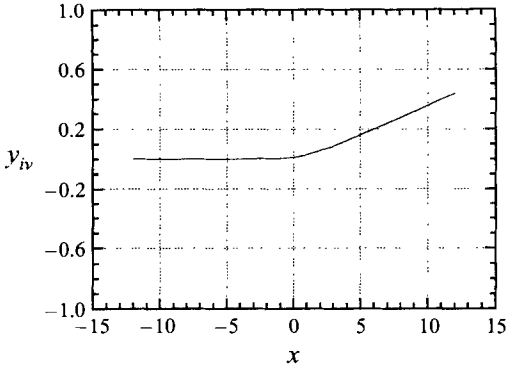

FIGURE 5. Theoretical vortex path for $K = 0.089$.

line. However, the model accuracy can be improved if the vortex path computed above is used to solve the problem again. A new pressure distribution and a new vortex path would be obtained, and an iterative procedure could be established. This scheme would be necessary only from an analytical point of view. The boundary condition (10*b*) is related to the vortex path. Since it is not known beforehand, it needs to be guessed. Thus, by solving the problem analytically a second time, the path of figure 5 would furnish a more accurate boundary condition. This new solution, however, is not expected to differ very much from the solution obtained here, since the comparison with experimental results, discussed in §4, shows good agreement.

A final consideration about the vortex-path results concerns a finite-chord wing. The continuous growth of the lateral vortex displacement, shown in figure 5, is a consequence of the lack of a trailing edge in the model. In a real flow, there will be a transition from the straight line with slope $\frac{1}{2}K$ (above the surface) to an approximately straight line with zero slope downstream from the trailing edge. This is expected to happen because, far upstream and far downstream from the edges, a finite chord wing will have a small effect on the vortex curvature. Since the vortex must follow a streamline, it must align with the uniform flow. Just a lateral displacement between the vortex positions far upstream and far downstream will exist.

3. Experimental set-up

A number of experiments were conducted in the Cornell Environmental wind tunnel, including pressure and velocity measurements, helium-soap bubble flow visualization and oil-surface flow pattern visualization. In this section, a summary of the experimental procedure and set-up will be presented. More details can be found in Bodstein (1993).

The experimental set-up consists of a wing and a flat plate placed in the test section of the wind tunnel. It is a suction tunnel with an open circuit and a rectangular cross-section (1.092 m high and 1.219 m wide), whose maximum speed is about 30 m s^{-1}. The flow is uniform within 3% and the turbulence intensity is about 0.9% in the potential flow core. A general side-view sketch of the test section and the experimental set-up is shown in figure 6. A vortex is generated by a rectangular wing placed vertically along the centreline of the test section. The wing section profile is NACA 0012, with a 0.185 m long chord and a 0.920 m long span. The wing's angle of attack and span (immersed in test section) are allowed to change, in order to vary the vortex strength and height.

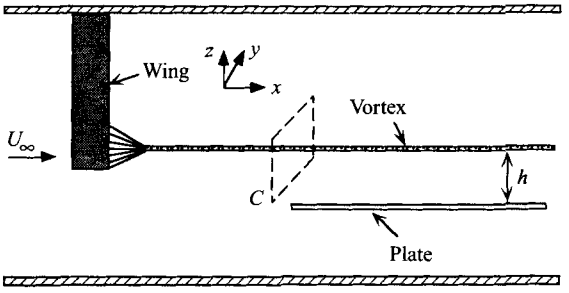

FIGURE 6. Schematic side view of the test section and the experimental set-up.

A plywood flat plate was placed horizontally in the test section, 5.5 wing chord lengths downstream of the wing. The plate spans the entire wind-tunnel width, and is 0.023 m thick and 1.346 m long. It was mounted 0.320 m above the wind-tunnel floor, well above the tunnel boundary layer. Its leading edge was rounded to minimize flow separation. The plate has 114 pressure taps placed along its spanwise direction, and distributed over five different chordwise stations located at 0.041 m, 0.187 m, 0.491 m, 0.797 m, 1.102 m (from the leading edge). The taps allow pressure measurements to be taken on the upper surface of the plate.

Pressure measurements were obtained by connecting the pressure taps to a data acquisition system. The pressure taps were hooked up with plastic tubing to the input ports of a scanivalve. The scanivalve used has two 24-port wafers, model W0602/1P-24T. The reference ports were connected to the static port of a Pitot-static tube, placed upstream in the wind tunnel, which provides the value of the free-stream speed. A Scanivalve CTLR10P/S2-S6 controller commands a solenoid, model WS5-25, which, in turn, drives the wafers. The scanivalve output ports were hooked up to two Omega PX-163 005BD5V pressure transducers, which send the output voltage to a Macintosh IIsi microcomputer. A National Instruments NB-MIO-16 data acquisition board is used for acquiring the data. Experimental data is taken using two channels, one for each pressure transducer. Measurements were taken at a sampling rate of 75 samples per second, for 20 s.

Velocity measurements were performed in the vortex flow field in order to determine the vortex strength (or circulation) and the velocity profile in the vortex core. Measurements were taken using a two-channel constant-temperature thermal hot-wire anemometer, model TSI 1047, with a TSI two-component $\times$-wire probe, model 1241. Mounted on a stepper motor-controlled two-component traverse the probe was aligned with the mean flow, and the measurements were taken in the (y, z)-plane that intercepts the plate's leading edge (see figure 6). Horizontal and vertical traverses across the flow were performed with the plate removed from the test section during the velocity measurements. The grid used for all the velocity measurements has 33 points per traverse in the y- and z-directions, with a mesh size of 0.005 m and a sampling rate of 200 samples per second, 10 s, for each grid point. The conversion from the anemometer's output voltage to effective cooling velocity was carried out using King's law, and the velocity components were determined following the procedure described by Fingerson, in chapter 4 of Goldstein (1983). The vortex strength, Γ, was calculated by numerically integrating the velocity field along the contour C, also shown in figure 6.

To visualize the vortex as helium-soap bubble flow experiment was performed using a multi-head bubble generator. The neutrally buoyant helium-soap bubbles were injected into the test section, in a region near the wing tip, and were visualized by

illuminating them from downstream of the test section. Several photographs were taken for different flow conditions. This experiment was also used to measure the actual distance h between the vortex and the plate, since the vortex tends to move upward owing to the presence of the plate and the rolling-up process of the wake at the wing tip.

Oil-surface flow pattern visualization experiments were carried out using a mixture of kerosene and lampblack, following the procedure described in Maltby & Keating (1962). The experiments were performed on a second plate model, built to preserve the pressure taps of the original model. In order to aid in the analysis of the boundary-layer topology on the surface, the locations of the separation and reattachment lines observed for some cases studied were measured with respect to the wind-tunnel walls, allowing a correspondence of the topology on the plate to the pressure measurements to be performed.

An uncertainty analysis was carried out for all the physical quantities measured in the experiments. The maximum uncertainty values obtained, for 95% coverage, were: $\Delta h = 3$ mm, $\Delta U_\infty = 0.01$ m s^{-1}, $\Delta \Gamma = 0.09$ m^2 s^{-1}, $\Delta K = 0.003$, $\Delta C_p = 0.0007$ (for some points near the suction peak $\Delta C_p = 0.002$).

4. Comparison between theoretical and experimental results

Two representative cases will be used to test the theory of §2. The test conditions are shown in table 1, with the interaction between the vortex and the plate becoming stronger as h decreases, or K increases, from case 1 to 2. The first column defines each case, and the next three columns contain the experimental values of the vortex strength, vortex height and free-stream speed, respectively. The remaining two columns show the corresponding values of the dimensionless vortex strength, K, and the Reynolds number based on the plate chord, Re_{pc}. In both cases studied the boundary layer on the plate is turbulent. If it is assumed that the boundary layer is two dimensional and the transition from a laminar to a turbulent flow occurs at a Reynolds number of 10^5, the point of transition would occur 53 mm downstream of the plate's leading-edge, i.e. near the first row of pressure taps.

4.1. *Velocity measurements*

For completeness we present in this section horizontal and vertical velocity traverses across the vortex core. Although our model does not account for core effects, these results may be useful to validate future numerical simulations of this problem. Axial and circumferential velocity profiles are shown in figure 7, for $\Gamma = 2.72$ m^2 s^{-1}. The velocity components were normalized by the free-stream velocity, and the y- and z-coordinates by the vortex core diameter. The vortex core diameter was defined as the length of the region between the maximum absolute values of the circumferential velocity component. According to this definition, the core diameter, d_v, was found to be 30 mm. The Reynolds number based on the wing chord is 3.5×10^5.

Inspection of figure 7(*a*) shows some important features of the vortex. First, the axial velocity profile is jet-like, with the velocity in the vortex core reaching a value at the centreline 1.5 times higher than in the potential flow. Batchelor (1964) developed a theoretical model for the velocity field of a trailing vortex far downstream of a wing and found a wake-like axial velocity distribution. Hall (1964) discussed Batchelor's solution and pointed out that the effect of the swirl is to cause a wake-like distribution to develop even if the axial velocity is initially jet-like. In fact, a recent study of the near-field of a wing-tip vortex carried out by Chow, Zilliac & Bradshaw (1993) reports

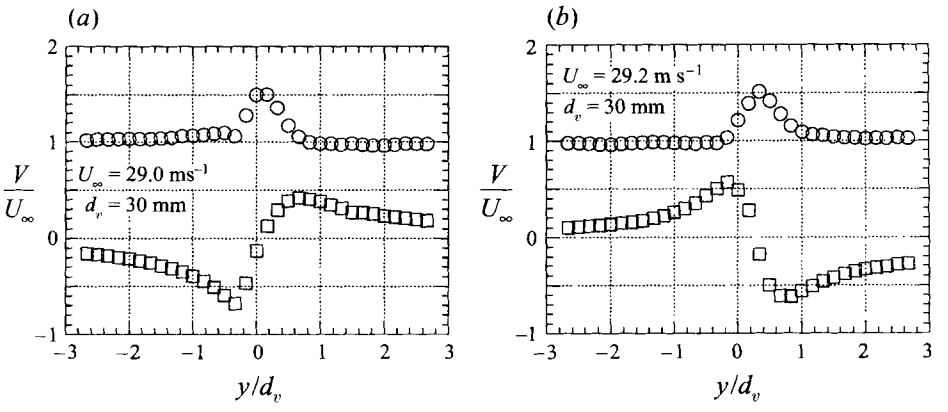

FIGURE 7. ○, Axial and □, circumferential velocity components across the vortex core: $\Gamma = 2.72$ m^2 s^{-1}. (*a*) Horizontal traverse; (*b*) vertical traverse.

	Γ (m^2 s^{-1})	h (mm)	U_∞ (m s^{-1})	K	Re_{pc}
Case 1	2.72	162	30.10	0.089	2.53×10^6
Case 2	2.71	20	29.90	0.720	2.52×10^6

TABLE 1. Cases studied.

axial velocities in the core as high as $1.8U_\infty$ at the centreline, at a location $x/c_w = 1.42$ behind the wing, where c_w is the wing chord. In figure 7 the measurements were made at $x/c_w = 5.5$, still in the near field of the vortex, to simulate a close-coupled canard-wing configuration.

Further observation of figure 7(*a*) indicates that the vortex is still not fully developed. The circumferential velocity profile shows a slight lack of symmetry along the radial direction. Near the point of maximum velocity, on the left-hand side of the vortex centreline, the velocity distribution is sharper than on the other side. Inspection of figure 7(*b*) shows that both the axial and the circumferential velocities are smoother and more symmetric than in figure 7(*a*). The velocity profiles are, therefore, dependent upon the angle around the vortex centreline.

4.2. *Helium-soap bubble flow visualization*

Figure 8 shows photographs of the flow visualization experiment using the helium-bubble technique, taken, however, at a lower free-stream speed (7.00 m s^{-1}) than in the other experiments. They are side-view pictures, with the mean flow moving from left to right. As described in §3, the bubbles were injected in the free-stream near the wing tip, which cannot be seen in the pictures. The vortex, part of its wake, and the upper surface of the plate were illuminated from downstream of the test section. The vertical bar in the middle of the pictures is the frame of the test section lateral door. When viewed from downstream, the vortex is rotating in a counterclockwise direction. Figures 8(*a*) and 8(*b*) correspond to cases 1 and 2, respectively. Figure 8(*c*) corresponds to the same case as figure 8(*b*), viewed from a different angle.

The first case considered, figure 8(*a*), represents the weak interaction case. It shows a steady vortex passing over the plate. There is no direct contact between the vortex core and the plate's boundary layer. Some bubbles, released in the wing wake, follow

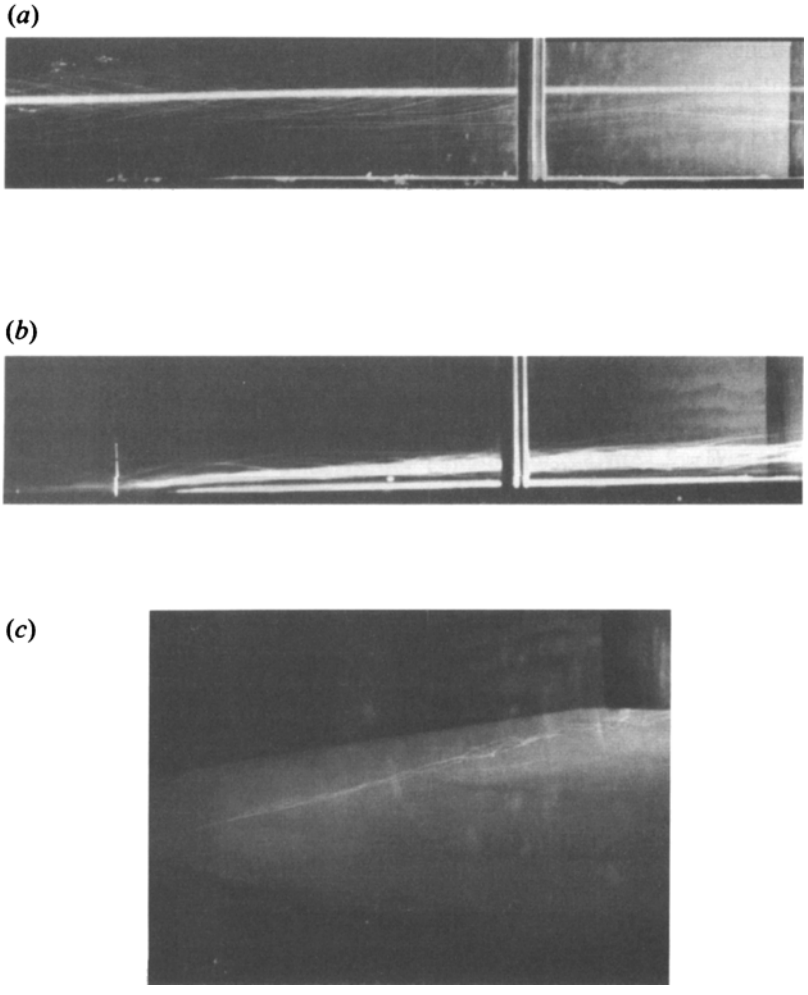

FIGURE 8. Results of the helium-soap bubble flow visualization experiment for cases 1 and 2. (*a*) Case 1; (*b*) case 2; (*c*) case 2: occurrence of vortex breakdown.

clearly a helical-like path around the core. The vortex path is very nearly rectilinear, indicating that the presence of the plate does not disturb the vortex in the vertical plane, as predicted by (40*b*). Mehta & Lim (1984) also found in their experiments, carried out for a low Reynolds number and a small-chord wing, that the vortex takes the no-vortex streamline trajectory (for weak interaction cases). Figures 8(*a*) and 8(*b*) corroborate this observation, even for different flow conditions. The flow in such cases is essentially inviscid.

For the strong interaction case, depicted in figure 8(*b*), the vortex seems to be in direct contact with the boundary layer, and viscous effects become important. Even in this case, the vortex vertical displacement is very small when it is passing above the wing. It is, however, non-negligible in the region between the wing and the leading edge of the plate. Near the leading edge, the vortex curves to avoid intercepting the plate, and only part of the core appears in the field of view. This effect may be attributed to the presence of the plate and the rolling-up process of the wing wake that forms the vortex. Figure 8(*b*) also shows some bubbles being ejected from the boundary layer, mainly in the region approaching the trailing edge of the plate. The core thickens as the vortex

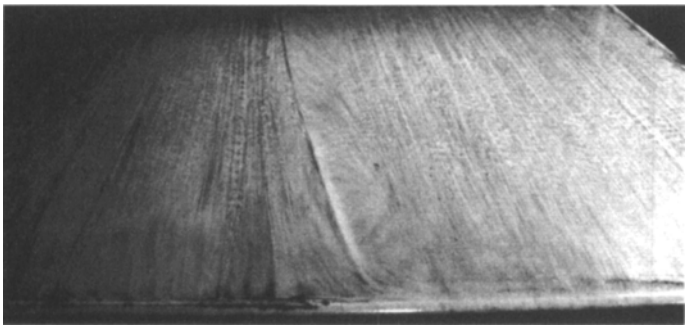

FIGURE 9. Results for the oil-surface flow pattern experiment.

passes over the plate, along the free stream direction. This effect is in part due to viscous interaction between the core and the boundary layer. It is also due to core instability.

Figure 8(*c*) also shows case 2, viewed from a different angle. Owing to the shorter exposure time used to take this picture, it is possible to see more clearly what is happening in the core: the occurrence of vortex breakdown. Good reviews of the vortex breakdown phenomenon can be found in Leibovich (1978) and Hall (1972). McAllister & Tung (1984) observed vortex instability in their experiments using hydrogen bubbles in a water tank. Patel & Hancock (1974), using smoke visualization, also observed vortex breakdown to occur. In both experiments the vortex breaks down at a position about half-chord above the wing, when the vortex passes very close to the surface. An estimate of the breakdown point based on figures 8(*b*) and 8(*c*) indicate that the breakdown point occurs at a free-stream position about a third of the chord downstream from the leading edge of the plate. It is also important to note that figure 8(*c*) shows the occurrence of the spiral type of vortex breakdown, which is the one observed in Patel & Hancock's experiments. Garg & Leibovich (1979) identified this type of vortex breakdown as the weakest form. The strongest form, the bubble type, produces a more violent core expansion and higher turbulence levels in the region downstream from the breakdown point. The flow conditions in figures 8(*b*) and 8(*c*) are apparently not strong enough to generate the bubble form.

4.3. *Oil-surface flow pattern visualization*

A selected result of the oil-surface flow pattern experiment is shown in figure 9 for case 2. The flow is moving from the bottom to the top of each picture. The vortex is rotating clockwise when seen from the camera's position, so that the right-hand side of the picture is the downgoing side of the flow. Although not shown here (see Bodstein 1993) tests were performed for case 1 and for the flow without the vortex, in order to assess the flow pattern on the upper surface of the plate. When the vortex is not present a small laminar separation bubble was observed to uniformly span the entire leading edge of the plate, followed by straight streamlines. This separation bubble was unsteady, indicating a turbulent reattachment localized close to the first row of pressure taps. For case 1, where the vortex is passing at a large distance over the plate, the streamlines on the surface of the plate were observed to be almost undisturbed by the presence of the vortex. Even though the separation bubble still exists over most of the leading edge, it was locally eliminated on the downgoing side of the vortex, near the centreline of the plate. The flow brings the stagnation line toward the upper surface of the plate and decreases the pressure gradient, which suppresses the occurrence of separation in that region and locally reduces the size of the separation bubble.

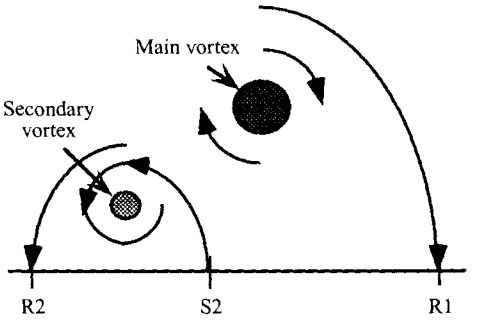

FIGURE 10. Conjectured front view schematic of the flow topology for case 2.

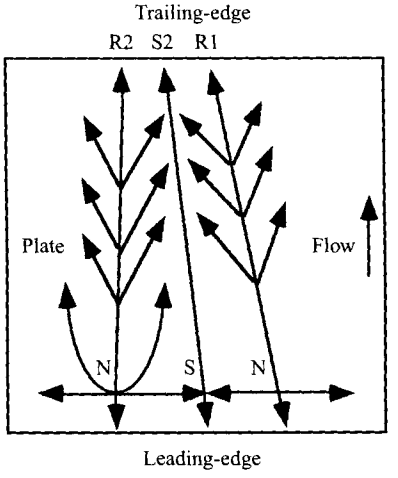

FIGURE 11. Leading-edge topology for case 2, N, node; S, saddle; R1, primary reattachment line; R2, secondary reattachment line; S2, secondary separation line.

For case 2, shown in figure 9, the strongest interaction takes place. It is likely that the vortex core is in direct contact with the plate's boundary layer, as pointed out in the previous section. The separation line starts to form at the leading edge, an extends over the entire upper surface of the plate. Near the trailing edge, along the fifth row of pressure taps, the separation line is displaced laterally by a large amount. This is evidence of a large vortex sideways movement. The interaction is so strong that the lampblack–kerosene mixture accumulates on the separated side of the line. Even though none of the flow-visualization techniques employed here were able to determine precisely the formation of a secondary vortex, the accumulation of mixture along the separation line strongly suggests that. This conjecture is supported by the herring-bone pattern built up between the separation and the secondary reattachment lines. The streamlines diverge from the reattachment line and converge toward the separation line, forming a herring-bone pattern. This pattern is characteristic of a flow that springs from the separation line to form a secondary vortex above the plate rotating in the opposite direction to the main vortex. Figure 9 also shows a secondary reattachment line on the left of the separation line (upgoing flow), and a primary reattachment line on the right (downgoing flow) formed owing to the main vortex. A conjectured sketch of the flow topology near the trailing edge is depicted in figure 10, where R1 stands for primary reattachment line, R2 for secondary reattachment line, and S2 for secondary separation line. The appearance of a two-dimensional secondary vortex in the

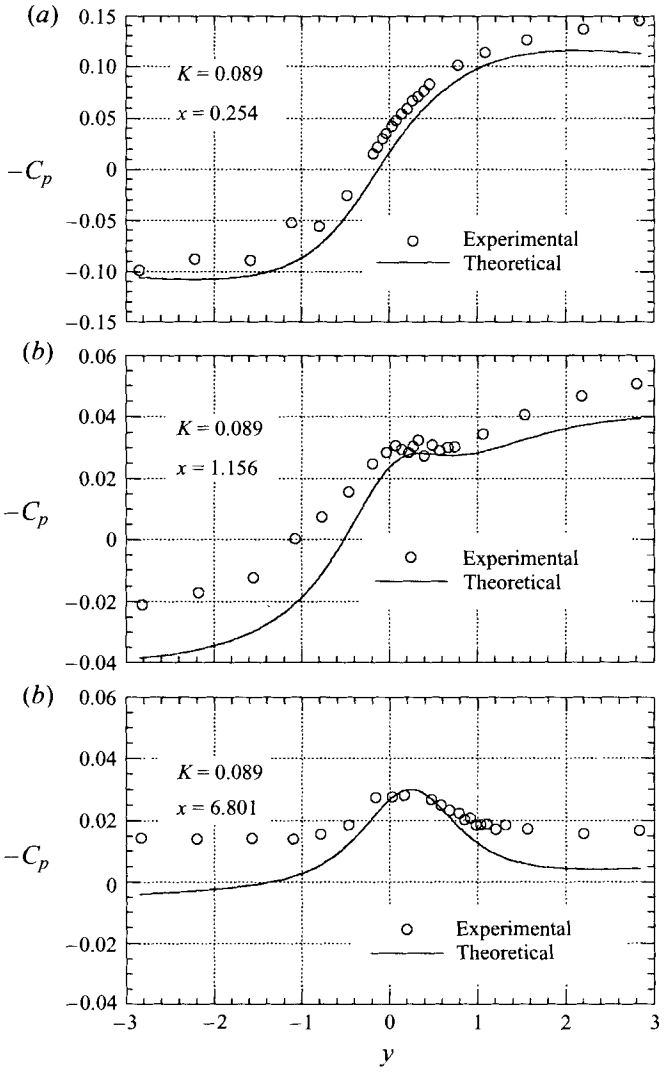

FIGURE 12. Case 1; $\Gamma = 2.720\ \mathrm{m^2\ s^{-1}}$, $h = 162$ mm, $U_\infty = 30.08\ \mathrm{m\ s^{-1}}$. (*a*) Row 1; (*b*) row 2; (*c*) row 5.

boundary layer of a flat surface owing to its interaction with a rectilinear vortex has been studied numerically by Doligalski & Walker (1984), Chuang & Conlisk (1989), and others. They report eruption of the boundary layer in the form of a secondary vortex owing to strong viscous–inviscid interaction.

The flow in the leading-edge region can also be examined in figure 9. On the right-hand side of the picture, where the flow moves downward, the separation bubble was completely suppressed in the region shown. On the upgoing side of the vortex, a large region of mixture accumulation can be seen, owing to the separation bubble. During the experiment this bubble was observed to be unsteady, pulsating at low frequency. A careful inspection of the flow topology at the leading edge indicates that a saddle point was the origin of the secondary separation line, and the reattachment lines originate at two nodes, one on each side. These critical points are connected to each other, as shown in figure 11, which is a qualitative top-view sketch of the streamline

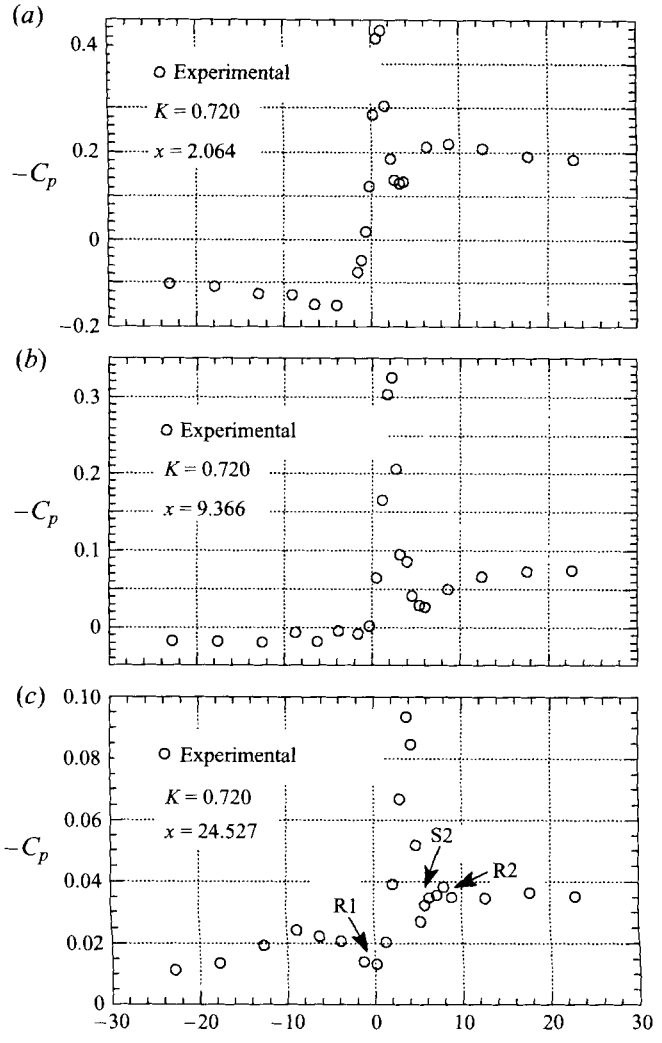

FIGURE 13(*a–c*). For caption see facing page.

pattern over the entire plate. Mehta & Lim proposed a similar conjectured topology for the leading-edge region of the wing used in their experiments. It is comprised of a saddle point and only one node as origins of the secondary separation and reattachment lines, respectively. They did not report the appearance of a primary reattachment line.

In summary, when the interaction is weak the flow is essentially invsicid, without any major disturbance. As the vortex approaches the plate, its interaction with the plate and its boundary layer becomes more and more intense, leading eventually to the occurrence of vortex breakdown and second separation over the plate. It should also be pointed out that, even for the case of strong interaction, the vertical vortex displacement, as it travels over the plate, was very small, except in the region upstream of the leading edge. This conclusion is in good agreement with the theoretical result of §2, namely, that the vertical vortex displacement is zero.

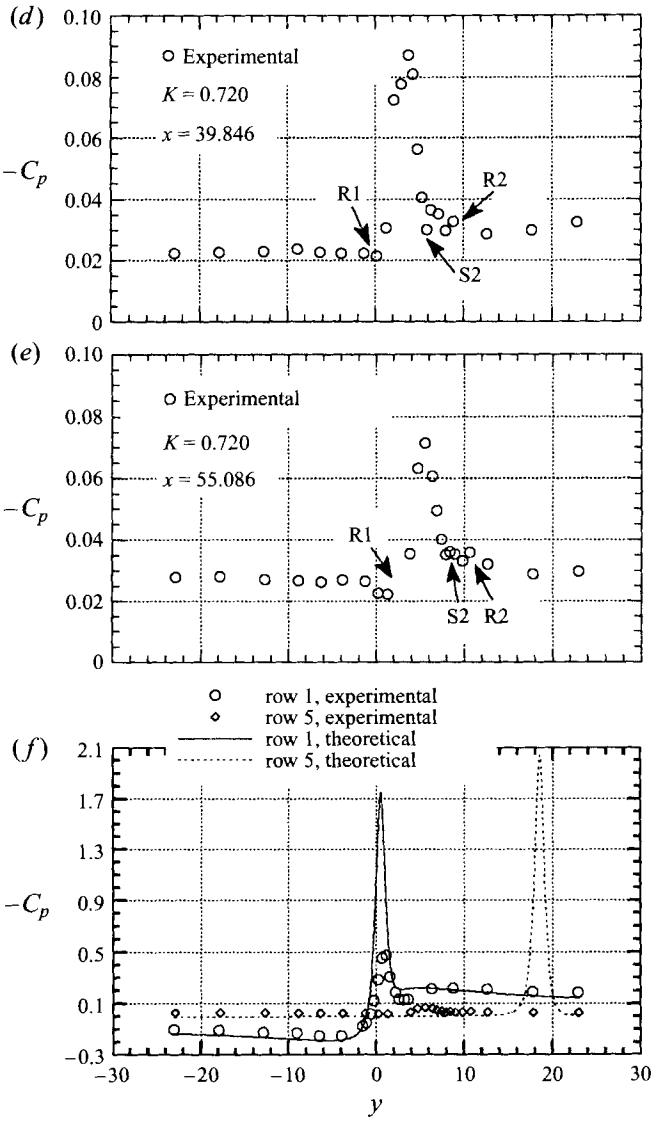

FIGURE 13. Case 2; $\Gamma = 2.706\ \mathrm{m^2\ s^{-1}}$, $h = 20$ mm, $U_\infty = 29.92\ \mathrm{m\ s^{-1}}$. (*a*) Row 1; (*b*) row 2; (*c*) row 3; (*d*) row 4; (*e*) row 5; (*f*) comparison of the theoretical and experimental pressure distributions.

4.4. *Pressure distributions*

Figures 12 and 13 show theoretical and experimental results for $-C_p$ plotted as a function of the spanwise coordinate, for several chordwise stations (each station corresponding to a row of pressure taps). The theoretical vortex path correction was incorporated to the theoretical pressure distributions. This procedure allows both the pressure distribution and the lateral vortex displacement to be compared on the same graph.

Figure 12 shows the results for case 1, the weak interaction case. In figure 12(*a*), the theoretical pressure distribution for the first chordwise station, $x = 0.254$, presents essentially an anti-symmetric behaviour, in good agreement with the experimental

results. Even though this station is very close to the leading-edge bubble observed in the oil-surface flow pattern results, the flow in this case is essentially inviscid, without any major viscous or nonlinear effects being important.

In figures 12(*b*) and 12(*c*) the experimental and theoretical pressure distributions are shown to have the same shape. As the flow moves to the chordwise stations further downstream it slowly changes from the anti-symmetric behaviour observed in figure 12(*a*) to a symmetric behaviour. Figure 12(*b*) shows this transition occurring. It can be seen from figures 12(*b*) and 12(*c*) that the experimental boundary between these two effects occurs downstream of the second row of pressure taps, which is consistent with the prediction of the theoretical model ($x_b = 1.96$). The results for the fifth chordwise station shown in figure 12(*c*) indicate that both the theoretical and experimental pressure distributions are symmetric, with the two suction peaks coinciding. However, the theoretical distribution is lower than the experimental one in regions away from the centreline, which produces a higher pressure variation along the span. In other words, the theoretical results predict well the pressure coefficient underneath the vortex, where the pressure gradients are steeper. This is the most important region of the flow. Nevertheless, away from the centreline region, figure 12 shows that the theoretical pressure coefficient deviates from the experimental one by an average value of 0.02. For a constant spanwise position, say $y = 2$, this deviation translates into a growing relative error with the chordwise movement downstream. At the first row, the difference is about 15%; at the second row, it increases to about 22%; by the fifth row, it reaches approximately 67%. These relative error magnitudes are due to the differences between the experiments and the theoretical model, where the most important is the lack of a trailing edge in the model. In the experiments the presence of a trailing edge causes the flow to reduce the differences of the pressure variation in the spanwise direction and on the top and bottom surfaces as the trailing edge is approached, so that ΔC_p goes to zero at the trailing edge (Kutta condition). The lack of a trailing edge in the theoretical model precludes the Kutta condition from being satisfied, and, therefore, the theoretical pressure coefficient tends asymptotically to a symmetric distribution (equation (33)), instead of reaching a symmetric distribution at some chordwise station and, then, decreasing in order to satisfy the Kutta condition as the trailing edge is approached. Observation of figure 12(*c*) also shows that the theory predicts well the small lateral displacement of the vortex.

Case 2, the strongest interaction case, is shown in figure 13. The vortex in this case is probably in direct contact with the plate's boundary layer where viscous effect are expected to be important, as revealed by the flow-visualization experiments. In this case, the experimental results are first plotted separately (figures 13*a–e*), and their comparison with the theoretical results for the first and fifth rows can be seen in figure 13(*f*). Examining figure 13(*a*), it can be seen that the experimental pressure distribution already has a well-developed suction peak at chordwise station 1, indicating that the anti-symmetric effect is dominated by the symmetric one. By station 2 the pressure distribution is almost entirely symmetric (figure 13*b*). However, at the third chordwise station, a secondary suction peak starts to develop on the right-hand side of the main peak, as shown in figure 13(*c*). The herring-bone pattern observed in the flow visualization experiments support the hypothesis that a secondary vortex was formed. The locations of reattachment and separation lines obtained from the oil-surface visualization experiment are indicated in figures 13(*c*)–13(*e*), for comparison with the pressure distribution. The small suction peak observed at station 3 increases in lateral extent as the flow moves downstream to station 4. By the fifth row of pressure taps, the pressure distribution becomes almost flat on the right-hand side of the main

peak, which suggests a possible interaction between the primary and the secondary vortices and an eventual merging process in progress. Examination of the suction peak for each row of pressure taps indicates that the largest decrease in $-C_p$, 0.23, occurs between rows 2 and 3. As discussed in §4.2, figure 8(*c*) shows the occurrence of vortex breakdown at approximately a third of the chord length downstream from the leading edge, which also falls between rows 2 and 3. This aids in understanding why the suction peak decreases dramatically in this region. The remaining drops in suction peak between rows of taps may be attributed to viscous interaction and the proximity of the trailing edge. The experimental results for rows 1 and 5 are replotted in figure 13(*f*) together with the theoretical prediction for this case. Because of the very strong interaction that takes place the value of $-C_p$ is well above the measured values. The theoretical vortex path also yields an unrealistically large lateral displacement by the fifth station. In summary, the theoretical analysis developed in §2 fails to predict accurately the pressure distribution for this case of strong interaction, although it still predicts well the shape of the pressure distribution.

5. Conclusions

The problem of the interaction of a streamwise vortex with a lifting surface, as it occurs in the flow around a close-coupled canard-wing configuration, was considered. A potential flow model was formulated and solved analytically for the flow on the surface. The solution shows a square-root singularity at the leading edge and the correct asymptotic behaviour as x tends to infinity. The pressure distribution demonstrates that the vortex causes two effects on the surface: an approximately anti-symmetric loading distribution near the leading edge, and a symmetric suction peak downstream from the leading edge. The anti-symmetric effect is shown to be proportional to the dimensionless vortex strength K, whereas the symmetric effect turns out to be proportional to the square of this quantity. Therefore, as the value of K increases, the symmetric effect dominates, and the lift force on the surface also increases. The lift coefficient per unit chord is shown to approach $\frac{1}{2}\pi$ as $x \to \infty$, which is an upper bound. The effect of vortex displacement caused by the surface vorticity field was also calculated and it shows that the vortex becomes laterally distorted in order to follow a streamline of the flow.

An experimental apparatus was set up to study this flow. The experimental results show an anti-symmetric pressure distribution on the surface near the leading edge, which gradually becomes symmetric downstream from it. When the interaction is weak all the physical trends observed in the experiments were also captured by the theory. The theoretical analysis shows good agreement for $-C_p$, but it starts to deviate from the experimental values when the symmetric suction effect is dominant, which occurs at chordwise stations far from the leading edge. The vortex trajectory obtained from the experiments compared well with the results calculated from the theory, as well as the boundary between symmetric and anti-symmetric effects. As the interaction becomes strong, or as K increases, viscous effects become important, where vortex core/boundary-layer interaction, secondary separation, and vortex breakdown occur. Also, the lateral vortex displacement over the surface was observed to be very large, whereas the vertical displacement is small. The theoretical model, in this case, overestimates the experimental suction peak and does not predict the viscous effects.

The authors would like to acknowledge the assistance and suggestions of the other members of the Aeroacoustics Research Group at Cornell University including

Edward Duell, Ben Sim and David Polak. Also the following undergraduate and MEng students helped with the experiments: William Brandt, John Cotter, Dean Head, Kevin Maki and Jaime Estupiñan, G.C.R.B. also acknowledges CNPq, a Brazilian Government Agency, for its sponsorship. A.R.G. acknowledges the partial support by NASA Langley under contract NAS1-19145 and Grant NAG-1-1396, and the Cornell-NASA Space Grant Program. C.Y.H. acknowledges the support of the Cornell Material Sciences Center which is funded by the NSF-DMR-MRL program.

REFERENCES

BARROWS, T. M. 1977 Simplified methods of predicting aircraft rolling moments due to vortex encounters. *J. Aircraft* **14**, 434–439.

BATCHELOR, G. K. 1964 Axial flow in trailing vortices. *J. Fluid Mech.* **20**, 645–658.

BODSTEIN, G. C. R. 1993 A theoretical and experimental study of the interaction of a streamwise vortex with a surface. PhD thesis, Cornell University, USA.

BODSTEIN, G. C. R., GEORGE, A. R. & HUI, C.-Y. 1993 Vortex/surface interaction. *AIAA Paper* 93-0863.

CARRIER, G. F., KROOK, M. & PEARSON, C. E. 1983 *Functions of a Complex Variable – Theory and Technique*. Hod Books.

CHOW, J. S., ZILLIAC, G. G. & BRADSHAW, P. 1993 Measurements in the near field of a turbulent wingtip vortex. *AIAA Paper* 93-0551.

CHUANG, F.-S. & CONLISK, A. T. 1989 The effect of interaction on the boundary layer induced by a convected rectilinear vortex. *J Fluid Mech.* **200**, 337–365.

DOLIGALSKI, T. L. & WALKER, J. D. A. 1984 The boundary layer induced by a convected two-dimensional vortex. *J. Fluid Mech.* **139**, 1–28.

FILOTAS, L. T. 1971 Solution of the lifting line equation for twisted elliptic wings. *J. Aircraft* **8**, 835–836.

GARG, A. K. & LEIBOVICH, S. 1979 Spectral characteristics of vortex breakdown flowfields. *Phys. Fluids* **22**, 2053–2064.

GOLDSTEIN, R. J. 1983 *Fluid Mechanics Measurements*. Hemisphere.

HALL, M. G. 1964 The structure of concentrated vortex cores. *Prog. Aeronaut. Sci.* **7**, 53–110.

HALL, M. G. 1972 Vortex breakdown. *Ann. Rev. Fluid Mech.* **4**, 195–218.

HAM, H. D. 1975 Some conclusions from an investigation of blade–vortex interaction. *J. Am. Helicopter Soc.* October, pp. 26–31.

HANCOCK, G. J. 1971 Aerodynamic loading induced on a two-dimensional wing by a free vortex in incompressible flow. *Aeronaut. J. R. Aeronaut. Soc.* **75**, 413–416.

HARVEY, J. K. & PERRY, F. J. 1971 Flowfield produced by trailing vortices in the vicinity of the ground. *AIAA J.* **9**, 1659–1660.

HOEIJMAKERS, H. W. M. 1990 Modeling and numerical simulation of vortex flows in aerodynamics. *AGARD-CP*-494.

JONES, W. P. 1972 Vortex-elliptic wing interaction. *AIAA J.* **10**, 225–227.

JUNG, Y. & SEATH, D. D. 1988 Spanwise displacement of a line vortex above a wing – a simple calculation scheme. *J. Aircraft* **25**, 476–478.

LEIBOVICH, S. 1978 The structure of vortex breakdown. *Ann. Rev. Fluid Mech.* **10**, 221–246.

MCALLISTER, K. W. & TUNG, C. 1984 Airfoil interaction with an impinging vortex. *NASA Tech. Paper* 2273.

MCMILLAN, O. J., SCHWIND, R. G., NIELSEN, J. N. & DILLENIUS, F. E. 1978 Rolling moments in a trailing vortex flowfield. *J. Aircraft* **15**, 280–286.

MALTBY, R. L. & KEATING, R. F. A. 1962 The surface oil flow technique for use in low speed wind tunnels. *AGARDograph, AGARD-AG*-70, pp. 29–38.

MASKEW, B. 1983 Predicting aerodynamic characteristics of vortical flows on three-dimensional configurations using a surface-singularity panel method. *AGARD-CP*-342.

MEHTA, R. D. & LIM, T. T. 1984 Flow visualization study of a vortex/wing interaction. *NASA Tech. Memo.* 86656.

MILNE-THOMPSON, L. M. 1975 *Theoretical Hydrodynamics*, 3rd edn. Macmillan.

NOBEL, B. 1958 *Methods Based on the Wiener-Hopf Technique for Partial Differential Equations.* Pergamon.

PATEL, M. H. & HANCOCK, G. J. 1974 Some experimental results of the effect of a streamwise vortex on a two-dimensional wing. *Aeronaut. J. R. Aeronaut. Soc.* **78**(760), 151–155.

PRESS, W. H., FLANNERY, B. P., TEUKOLSKY, S. A. & VETTERLING, W. T. 1989 *Numerical Recipes – The Art of Scientific Computing (FORTRAN Version).* Cambridge University Press.

SEATH, D. D. & WILSON, D. R. 1986 Vortex–airfoil interaction tests. *AIAA Paper* 86-0354.

SILVER, L. W. 1966 An investigation of the interaction of a trailing vortex with a lifting-surface. MS thesis, MIT, Cambridge, MA, USA.

SMITH, W. G. & LAZZERONI, F. A. 1960 Experimental and theoretical study of a rectangular wing in a vortical wake at low speed. *NASA Tech. Note* D-339.

SRINIVASAN, G. R., CHYU, W. J. & STEGER, J. L. 1981 Computation of simple three-dimensional wing–vortex interaction in transonic flow. *AIAA Paper* 81-1206.

VAN DYKE, M. 1956 Second-order subsonic airfoil theory including edge effects. *NASA Rep.* 1274.

VAN DYKE, M. 1975 *Perturbation Methods in Fluid Mechanics.* Parabolic, Stanford, CA.